Supporting information

Liu et al. 10.1073/pnas.1218792109

SI Materials and Methods

Dot Blot Analysis. Dot blot analysis was performed as previously described (1). Briefly, 5 μL each sample at the concentration of 50 μM was spotted onto a nitrocellulose membrane (Bio-Rad Laboratories). After blocking in 10% (wt/vol) fat-free milk in Tris-buffered saline (TBST; 50 mM Tris, 150 mM NaCl, 0.05% Tween20) at room temperature for 1 h, the membranes were incubated with the rabbit polyclonal A11 antibody at 2.4 μg/mL in 5% (wt/vol) fat-free milk and TBST overnight at 4 °C. The membranes were washed three times in TBST and incubated with anti-rabbit HRP-conjugated secondary antibodies [1:5,000 in 5% (wt/vol) fat-free milk and TBST; Jackson ImmunoResearch Laboratories] at room temperature for 1 h. The blots were washed three times in TBST buffer and developed using the Super Signal West Pico Chemiluminescent Substrate Kit (Thermo Scientific). $A\beta_{1-40}$ prefibrillar oligomers and fibrils were used as positive and negative control for A11 immunoreactivity.

Pulsed Field Gradient NMR Diffusion Coefficient Measurements. DOSY (Diffusion Ordered SpectroscopY) experiments of β-sheet amyloid mimic (BAM) ($A\beta_{30-36}$) included a series of 16 pulsed field gradient spin-echo experiments that were carried out with a 75-ms delay. The gradient strength of these DOSY experiments was incremented to allow *ca.* 2–95% signal attenuation with a linear ramp (2). Data were processed to give a pseudo-2D spectrum, and the diffusion coefficients of BAM ($A\beta_{30-36}$) were read from the spectrum after careful phasing and calibration (the diffusion coefficient of residual HOD in D_2O: 1.9×10^{-9} m^2/s at 298 K).

X-Ray Fibril Diffraction. The fibril samples were obtained by incubation of the BAMs in PBS buffer (pH 7.4) at 37 °C with continuous shaking for 10 d. The fibril samples were concentrated by centrifugation followed by washing with water two times to remove the salts in PBS buffer. Then, the pellets were resuspended into 5 μL water. The suspension was pipetted, aligned, and dried between two fire-polished glass rods for several hours. Finally, the fibril samples were mounted on the in-house X-ray machine using a Rigaku FR-D X-ray generator equipped with an RIGAKU HTC Imaging plate detector. The diffraction data were collected with 5° rotation oscillation for 5-min exposures.

Cell Viability Assays. The MTT assay was performed for cell viability test by using the CellTiter 96 nonradioactive cell proliferation assay kit (Promega). The toxic effect of aggregates formed by BAMs and amyloidogenic peptides was assessed in HeLa cells and PC-12 cells (CRL-1721; ATCC). Cells were maintained at 37 °C in 5% (vol/vol) CO_2, and they were cultured in ATCC-formulated RPMI medium 1640 (30–2001; ATCC) with 10% (vol/vol) heat-inactivated horse serum and 5% (vol/vol) FBS for PC-12 cells and DMEM with 10% (vol/vol) FBS for HeLa cells. For all cell viability experiments, 96-well plates (3596; Costar) were used. Before reagent treatment, HeLa and PC-12 cells were plated out at 10,000 cells/well and cultured for 20 h at 37 °C in 5% (vol/vol) CO_2. For the samples tested in the assay, the amyloidogenic peptides were synthesized by Celtek Bioscience Peptides. BAMs were synthesized by using the method reported previously (3). Before toxicity test, all of the BAMs oligomers samples were incubated in PBS buffer at 37 °C with shaking for 0.5 h. For fibril sample preparation, amyloidogenic peptide KDWSFY (β_2m_{58-63}) with the concentration of 30 mg/mL was incubated in 75 mM sodium citrate buffer (pH 6.0) for 4 d in the presence of 5% (vol/vol) seeds. Seeds were prepared by sonication of preformed KDWSFY ($\beta 2m_{58-63}$) mature fibril, which was obtained by incubation of 30 mg/mL peptide in sodium citrate buffer (pH 6.0) at 37 °C with shaking for 30 d. Before MTT [3-(4,5-Dimethylthiazol-2-yl)-2,5-diphenyltetrazolium bromide] assay, the fibril sample was then diluted into PBS buffer. Other short peptides and BAMs were incubated in PBS buffer for 4 d at 37 °C with shaking. Fibrils formed after 4 d were confirmed by transmission EM (Fig. 3*A* and Fig. S2). To start the assay, 10 μL sample were added to each well containing 90 μL medium; 15 μL Dye solution (G4000; Promega) were added into each well after 24 h of the incubation period followed by further incubation for 4 h at 37 °C in 5% (vol/vol) CO_2. Then, 100 μL solubilization Solution/Stop Mix (G4000; Promega) were added to each well. The absorbance was measured at 570 nm after 12 h incubation at room temperature to fully solubilize the dye molecules. The background absorbance was recorded at 700 nm. Four replicates were measured per sample. The readout from the PBS buffer-treated cell is regarded as 100% viability, and the readout from the 0.2% treated cell is treated as 0% viability.

Rosetta Modeling. ***a. Rosetta threading of other BAMs fibril structures.*** Using Rosetta package (4), various amyloidogenic sequences were threaded into the backbone templates of BAM (β_2m_{62-68}) and BAM ($Tau_{305-311}$) structures. Guided by Rosetta full-atom energy functions, the fibril structures were refined by simultaneously optimizing degrees of freedom on (*i*) the rigid-body geometry between symmetrical copies, (*ii*) backbone torsions of each peptide, and (*iii*) side chain torsions of each peptide. Taking advantage of the recently developed symmetry implementation in Rosetta (4, 5), the fibril symmetry was restrained to assure that symmetrical geometry is satisfied during the whole optimization process. The lowest-energy model was picked by the sum of the attractive portion of nonbond Lennard–Jones potential, LK implicit solvation energy (6), and orientation-dependent hydrogen-bonding interaction (7). The sequences of the BAM templates (β_2m_{62-68} and Tau_{305-31}) were also threaded into both backbone templates of BAM fibril structures, and their structures were refined through the same procedures as discussed above. The energies of all final models from different peptides sequences are listed in Table S5.

b. Rosetta building of BAM ($A\beta_{30-36}$) fibril models for molecular dynamic simulation. Using the same threading strategy as the one above, the fibril model of BAM ($A\beta_{30-36}$) was built by sampling possible out-of-register β-sheet fibril arrangements with different arrangement of register shift and fibril growing directions. Two of the lowest energy models were generated with two different preferential directions of fibril growth, and both models were subjected to energy optimization using CHARMM. Finally, the lowest-energy model after CHARMM energy optimization was picked up and underwent additional simulation and analysis.

c. Rosetta building of peptides and full-length $A\beta_{1-42}$. The starting models of the peptide segments, including fibrillar and oligomeric structures, were built using the Rosetta package. The initial backbone conformations were from crystal structure of amyloid peptides and cylindrins. The sequences were threaded into the initial backbone template followed by side chain rotamer optimization, and then, the whole structures were optimized by Rosetta backrub simulations together with side chain torsion and rigid-body minimization. The lowest energy models were chosen for additional simulation and analysis.

d. Molecular dynamics simulation for the peptide KDWSFY(β_2m_{58-63}) using Rosetta models. To explore the energy landscape of two aggregation pathways (in-register and out-of-register pathways) of am-

yloid peptides, we took the peptide KDWSFY (β_2m_{58-63}) as a model system and performed molecular dynamics (MD) simulation for its possible transition/intermediate/fibril states in both pathways (Fig. S3). For each state, starting structures derived from either the crystal structures or the Rosetta modeling based on the homology structures were optimized by 20-ns MD simulation with explicit water molecules. The MD models from each snapshot (every 200 ps) of each simulation are stored, and their free energies are calculated by the generalized born/surface area (GB/SA) method. The MD simulations identified two stable fibril states (in-register and out-of-register fibrils). The energies of MD models fluctuated up and down along both simulation trajectories, whereas their structures were fully sampled around the starting structure. The average free energy of each snapshot along MD simulation is used to represent the free energy of both simulation trajectories. The free energy of the KDWSFY monomer is also calculated by averaging the energies from all different MD snapshots. On the contrary, MD simulation shows that KDWSFY cylindrin-like oligomer only maintains the original cylindrin structure for several nanoseconds simulation. MD simulations of in-register and out-of-register β-sheet pairs yield similar results. For these substable states (cylindrin, in-register, and out-of-register β-sheet pairs), their average free energies are based on the MD models with conformations that are close to the starting model (rmsd ≤ 3 Å). Moreover, we calculated the pairwise rmsd matrix between snapshot models from different simulations to check the possible overlap between different simulations. If any snapshot models from two different simulations share nearly identical structures (rmsd ≤ 0.5 Å), these two states are considered as ready conversions from each other.

MD Simulation and Free Energy Analysis. ***a. MD simulation of cylindrin and fibril models.*** Atomistic models of the cylindrin-like oligomer and fibrillar structures of BAM ($A\beta_{30-36}$) were modeled using Param22 force fields (8). Force field parameters for Hao were obtained from a web-server (http://www.paramchem.org), which is based on CGenFF force field (9) and integrated with neighboring peptides. The atomistic model of cylindrin was solvated in $90 \times 90 \times 90$-Å^3 solvation box filled with TIP3 water molecules. The fibril model consisted of 12 macrocycles. The model was solvated in a $87.42 \times 96 \times 96$-Å^3 solvation box, where the fibril axis aligned with the x axis of the box. Because of the periodicity of the simulation boundary, one end of the fibril contacted the other end, mimicking an infinitely long fibril. Both solvated systems incorporated chlorine ions to neutralize positive charges on peptides. We used NAMD v2.8 for MD simulation. Each system was heated from 0 to 300 K for 100 ps and equilibrated for 500 ps at 300 K. Lastly, 10-ns production runs were performed for each model, saving atomic coordinates every 2 ps. The bond length between a hydrogen and its donor was constrained using the Settle algorithm, which enabled 2-fs integration steps for the simulation. A constant pressure temperature algorithm controlled simulation temperature (pressure) at 300 K (1 atm) (10).

b. Molecular mechanics GB/SA approximation for free energy analysis. After finishing the constant pressure temperature MD simulation, the total free energy of each model was computed using molecular mechanics Generalized Born-Surface Area (MM-GB/SA) approximation (11). Total free energy of the molecule (G_{total}) is assumed to be a sum of energy terms:

$$G_{total} = E_{int} + E_{vdW} + E_{elec} + G_{np,solv} + G_{polar,solv} - TS_{rot} - TS_{trans},$$

where E_{int} represents the sum of covalent bonding energy terms (bond, angle, dihedral, and improper dihedral), E_{vdW} is van der Waals energy, E_{elec} is electrostatic energy in vacuum, $G_{np,solv}$ is nonpolar solvation energy that is proportional to solvent accessible surface area of the solute with a proportionality constant (σ = 5 cal mol^{-1} Å^{-2}), and $G_{polar,solv}$ is polar solvation energy approximated by the GB solvation model. We used an implementation of the GB solvation model in Charmm v36. Entropic contributions, S_{rot} and S_{trans}, account for rotational and translational degrees of freedom of solutes in solution. Unlike the original form of molecular mechanics MM-GB/SA, we ignored vibrational entropic contribution of the solute, which contributes only a minor fraction in the total free energy difference in comparing distinct conformational states of a macromolecule (12).

c. Targeted MD simulation. Targeted MD (TMD) simulation (13) was aimed at understanding the detailed structural conversion mechanism and intermediate conformations along the pathway from the cylindrin-like oligomer BAM ($A\beta_{30-36}$) to the short fibril. We took the cylindrin-like oligomer and four macrocycles from the fibril model as the target conformations for TMD. Initially, the cylindrin-like oligomer was immersed in a $90 \times 90 \times 90$-Å^3 solvation box. After heating (100 ps) and equilibrating (500 ps) periods, each heavy atom coordinate was gradually converted to the coordinate of the short fibril by adopting a constraining potential:

$$U(\vec{r},t) = \frac{k}{2}(RMSD(\vec{r},t) - RMSD^*(t))^2,$$

where the strength of constraining potential (k) is 200 pN Å^{-2}, $\vec{r}$ is an all-heavy atom coordinate vector of cylindrin, $RMSD(\vec{r},t)$ is rmsd to the target structure at t, and $RMSD^*(t)$ is the instantaneous target rmsd linearly decreased from its initial value to zero in 10 ns (forward simulation). During the next 10 ns, the conformation was reversed to its original conformation (reverse simulation).

d. Umbrella sampling simulation and Gibbs free energy analysis. TMD simulation suggested that the dissociation of the weak interface hydrogen bonds initiates structural conversion of cylindrin to the out-of-register fibril. This finding motivated us to consider the detailed energetics associated with the transition. We carried out umbrella sampling MD simulation (14) along the proposed structural conversion pathway of a cylindrin to compute the Gibbs free energy change with accuracy. Relative Δrmsd of all heavy atoms from two of the target conformations (cylindrin and short fibril) was chosen as the reaction coordinate of the transition. The interval between minimum and maximum values of the reaction coordinate (−5.68 to 5.68 Å) was divided into 26 equally spaced windows. We performed two sets of umbrella sampling simulations. For the first set, starting conformation of each window was chosen as the lowest energy conformation assigned to the window from the forward TMD simulation. For the second set, starting conformation of each window was chosen as the lowest energy conformation assigned to the window from the reverse TMD simulation. Each starting conformation was heated from 200 to 300 K in 100 ps, while constraining all heavy atoms to their starting positions. Then, we carried out the 2.5-ns MD simulation with an umbrella potential with a minimum that was aligned with the center of corresponding window:

$$U_i(\vec{r},t) = \frac{k}{2}(RMSD_1(\vec{r},t) - RMSD_2(\vec{r},t) - \delta_i)^2,$$

where i is the index of windows ($i \in \{n | 1 \le n \le 26\}$), k = 20 pN/Å is the strength of the umbrella potential, and δ_I is the offset of the ith window, which is centered at the middle of the window. We monitored the conformational energy and Δrmsd coordinate every 0.2 ps and saved atomic coordinates every 2.0 ps. Finally, we integrated the energy histogram and Δrmsd coordinate trajectory using the weighted histogram analysis method (15) to produce the Gibbs free energy profile along the reaction coordinate. We used the last 2.2 ns data of each window, regarding

the first 0.3 ns as a relaxation period. Two sets of simulation data were joined over an overlapping region. The overlapping region on the reaction coordinate was selected based on structural similarity of the sampling: we compared the 2D rmsd profile ($RMSD_1$, $RMSD_2$) of both simulations and determined windows encompassing similar conformations. Consequently, we chose windows 10–16 as the overlapping region. The integrated free energy profile was plotted on a 2D surface as a function of rmsd from two of the target conformation using the SciPy package (16) for the 2D heat map (Fig. S7). In addition, a hierarchical clustering algorithm was applied to cluster sampled structures based on their structural similarity (17). We depicted the representative conformation of the lowest free energy cluster of native, transition, and intermediate conformations in Fig. S7.

Out-of-Register Fibril Model Building and Fibril Diffraction Simulation. To investigate the difference of the diffraction pattern between an out-of-register antiparallel steric zipper and an in-register antiparallel steric zipper, fibril models were constructed in a large P1 unit cell ($a = c = 300.0$, $b = 11.73$ Å with angles of 90°) and oriented so that the fibril axis corresponds to the b dimension of the unit cell. The starting model contained ideal β-strands generated by the program MOLEMAN. The side chains were mutated using the program COOT to the sequence FSKDWSFYLLY corresponding to residues 56–66 of human β_2m. For the out-of-register fibril model, the unit cell contained two pairs of antiparallel out-of-register β-strands with class 5 symmetry (18) mimicking the symmetry of the KDWSFY peptide crystal structure described in this paper. For the in-register fibril model, two pairs of antiparallel in-register β-strands with class 5 symmetry are built. Unit cell translations in the positive and negative b dimension created a pair of six-stranded antiparallel out-of-register β- or in-register sheets. The models were energy-refined using conjugate gradient and simulated annealing algorithms of the program CNS (19) as well as a hydrogen-bond potential (20). The simulated fibril diffraction pattern was prepared by cylindrically averaging the single-crystal diffraction pattern calculated by the CCP4 program SFALL. The diffraction pattern is averaged around the fibril axis by 360°, and then, the pattern is blurred by 60° around the beam direction to mimic the imperfect alignment of the fibrils.

1. Kayed R, et al. (2003) Common structure of soluble amyloid oligomers implies common mechanism of pathogenesis. *Science* 300(5618):486–489.
2. Wu DH, et al. (1995) Flow imaging by means of 1D pulsed-field-gradient NMR with application to electroosmotic flow. *J Magn Reson A* 115:123–126.
3. Cheng PN, Liu C, Zhao ML, Eisenberg D, Nowick JS (2012) Amyloid β-sheet mimics that antagonize protein aggregation and reduce amyloid toxicity. *Nat Chem* 4(11): 927–933.
4. André I, Bradley P, Wang C, Baker D (2007) Prediction of the structure of symmetrical protein assemblies. *Proc Natl Acad Sci USA* 104(45):17656–17661.
5. Leaver-Fay A, et al. (2011) ROSETTA3: An object-oriented software suite for the simulation and design of macromolecules. *Methods Enzymol* 487:545–574.
6. Lazaridis T, Karplus M (1999) Effective energy function for proteins in solution. *Proteins* 35(2):133–152.
7. Kortemme T, Morozov AV, Baker D (2003) An orientation-dependent hydrogen bonding potential improves prediction of specificity and structure for proteins and protein-protein complexes. *J Mol Biol* 326(4):1239–1259.
8. MacKerell AD Jr., et al. (1998) All-atom empirical potential for molecular modeling and dynamics studies of proteins. *J Phys Chem B* 102(18):3586–3616.
9. Vanommeslaeghe K, et al. (2010) CHARMM general force field: A force field for drug-like molecules compatible with the CHARMM all-atom additive biological force fields. *J Comput Chem* 31(4):671–690.
10. Feller SE, Zhang Y, Pastor RW, Brooks BR (1995) Constant pressure molecular dynamics simulation: The Langevin piston method. *J Chem Phys* 103(11):4613.
11. Wang W, Kollman PA (2000) Free energy calculations on dimer stability of the HIV protease using molecular dynamics and a continuum solvent model. *J Mol Biol* 303(4): 567–582.
12. Park J, Kahng B, Hwang W (2009) Thermodynamic selection of steric zipper patterns in the amyloid cross-β spine. *PLoS Comput Biol* 5(9):e1000492.
13. Schlitter J, Engels M, Krüger P (1994) Targeted molecular dynamics: A new approach for searching pathways of conformational transitions. *J Mol Graph* 12(2):84–89.
14. Lee J, Kim YG, Kim KK, Seok C (2010) Transition between B-DNA and Z-DNA: Free energy landscape for the B-Z junction propagation. *J Phys Chem B* 114(30):9872–9881.
15. Kumar S, Rosenberg JM, Bouzida D, Swendsen RH, Kollman PA (1992) The weighted histogram analysis method for free-energy calculations on biomolecules. I. The method. *J Comput Chem* 13(8):1011–1021.
16. Jones E, et al. (2001) *SciPy: Open Source Scientific Tools for Python*. Available at http://www.scipy.org. Accessed February 2010.
17. Eads D (2008) *hcluster: Hierarchical Clustering for SciPy*. Available at http://scipy-cluster.googlecode.com. Accessed April 2010.
18. Sawaya MR, et al. (2007) Atomic structures of amyloid cross-beta spines reveal varied steric zippers. *Nature* 447(7143):453–457.
19. Brünger AT, et al. (1998) Crystallography & NMR system: A new software suite for macromolecular structure determination. *Acta Crystallogr D Biol Crystallogr* 54(Pt 5): 905–921.
20. Fabiola F, Bertram R, Korostelev A, Chapman MS (2002) An improved hydrogen bond potential: Impact on medium resolution protein structures. *Protein Sci* 11(6):1415–1423.

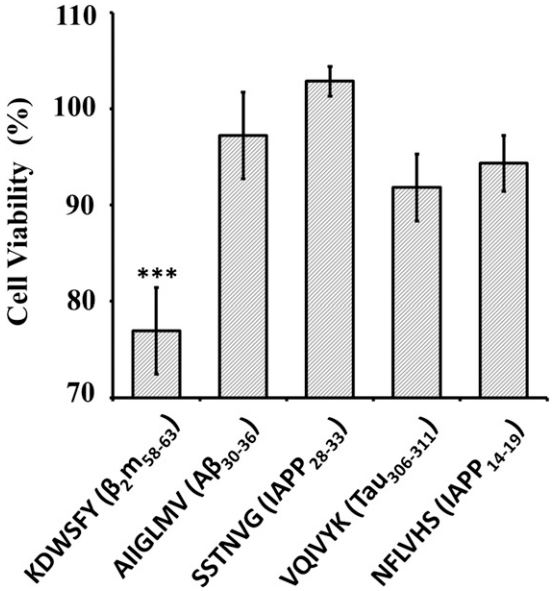

Fig. S1. Comparison of cytotoxicity of an out-of-register fibril (KDWSFY) with in-register fibrils (four). KDWSFY (β_2m_{58-63}) fibrils showed significant toxicity (***$P < 0.001$ as determined by one-sided Student *t* test) compared with the in-register peptide fibrils formed by AIIGLMV($A\beta_{30-36}$), SSTNVG($IAPP_{28-33}$), VQIVYK ($Tau_{306-311}$), and NFLVHS($IAPP_{14-19}$) (1–3) in the HeLa cell line as determined by one-sided Student *t* test (Table S2). Error bars represent 1 SD ($n = 4$). The concentration of each fibril sample is 100 μM (monomer equivalence). All fibril samples are prepared by incubating at 37° for 4 d with shaking. The formation of fibrils for each sample was confirmed by EM (Fig. S2).

1. Sawaya MR, et al. (2007) Atomic structures of amyloid cross-beta spines reveal varied steric zippers. *Nature* 447(7143):453–457.
2. Wiltzius JJ, et al. (2009) Molecular mechanisms for protein-encoded inheritance. *Nat Struct Mol Biol* 16(9):973–978.
3. Colletier JP, et al. (2011) Molecular basis for amyloid-beta polymorphism. *Proc Natl Acad Sci USA* 108(41):16938–16943.

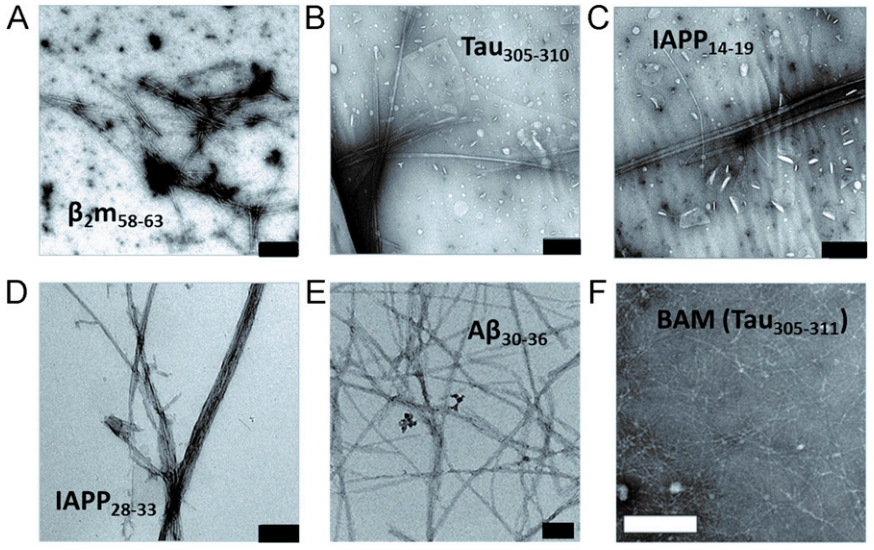

Fig. S2. Amyloid-like fibrils observed by negative-staining EM. Before transmission EM sample preparation, the amyloidogenic peptides and BAM ($Tau_{305-311}$) were incubated for 4 and 20 d at 37 °C with shaking, respectively. (Scale bars: *A*, 500 nm; *B–E*, 300 nm; *F*, 200 nm.)

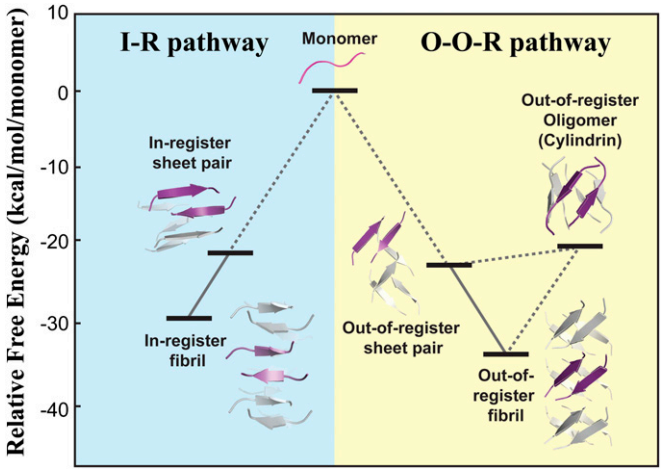

Fig. S3. Energy landscape of two aggregation pathways of the amyloid peptide KDWSFY (β_2m_{58-63}) explored by MD simulation. Two distinct pathways, in-register (I-R) and out-of-register (O-O-R), are proposed for the structural conversion from monomer to fibril (Fig. 6). We performed MD simulation with Rosetta modeling to sample six different states of KDWSFY initiated in either I-R (cyan background) or O-O-R pathways (yellow background) to investigate (*i*) which aggregation pathway would be energetically favorable for the KDWSFY fibril formation and (*ii*) whether a stable structure of the KDWSFY oligomer exists. The six possible states include (*i*) monomer, (*ii*) pair of in-register β-sheets, (*iii*) in-register fibril, (*iv*) out-of-register oligomer (cylindrin), (*v*) pair of out-of-register β-sheets, and (*vi*) out-of-register fibril. All of the states are aligned by their average free energies. The free energy of the KDWSFY monomer, highest among all of the states, is set to zero. Different states are connected by either a solid line (MD simulation trajectories of the two connected states overlap) or a dotted line (hypothetical). As shown, the out-of-register fibril with the lowest free energy is thermodynamically more stable than the in-register fibril, which is in agreement with our experimental observation that KDWSFY exhibits the out-of-register β-sheets fibrillar structure in crystals. That is, the O-O-R pathway is more plausible for KDWSFY aggregation. We also focus on the formation of the KDWSFY out-of-register oligomer in the O-O-R pathway. The free energy of the KDWSFY oligomer is much higher (+13 kcal/mol) than the out-of-register fibril. The MD simulation shows that the KDWSFY oligomer maintains the original cylindrin-like structure only for several nanoseconds, suggesting that the KDWSFY out-of-register oligomer is unstable and transient. This observation could explain why we are not able to capture the KDWSFY out-of-register oligomer in solution.

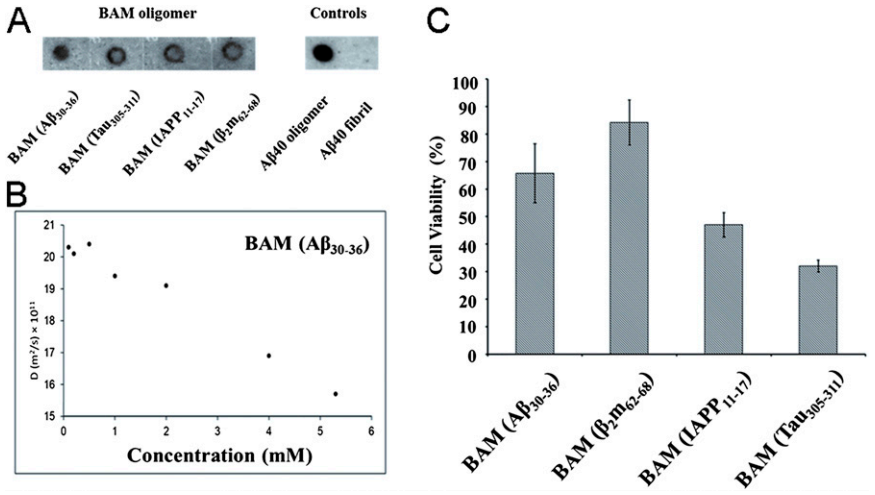

Fig. S4. Characterization of oligomeric BAMs. (*A*) Immuno-dot blot analysis of BAM oligomers with amyloid oligomer-specific polyclonal antibody A11. All four BAM oligomers are recognized by A11, suggesting that they share common structural features with other amyloid oligomers. Amyloid (β_{1-40}) fibrils and oligomers are used as negative and positive controls, respectively. (*B*) NMR studies in D_2O show that BAM ($A\beta_{30-36}$) self-associates in a concentration-dependent fashion consistent with the formation of oligomers; 1D NMR presat spectra of BAM ($A\beta_{30-36}$) at various concentrations ranging from 100 μM to 5.3 mM were acquired for calculating diffusion coefficients of BAM ($A\beta_{30-36}$) as a function of concentration. The diffusion coefficient was measured by 600 MHz DOSY experiments in D_2O at 298 K. At low concentrations (below 500 μM), BAM ($A\beta_{30-36}$) is largely monomeric, but it self-assembles on increasing concentration. At 5 mM, the observed diffusion coefficient is consistent with a model in which ca. 50% of BAM ($A\beta_{30-36}$) is present as a tetramer in rapid equilibrium with the monomer. (*C*) An MTT-based cell viability assay was used to assess the cytotoxicity of BAM oligomers with the PC12 cell line. All four BAM oligomers are toxic, killing between 15% and 70% cells. Error bars represent 1 SD (n = 4). Before carrying out immuno-dot blot and MTT tests, we prepared the BAM oligomer samples by dissolving BAMs to 1 mM and incubating them for 0.5 h at 37 °C. The final concentration of each sample of BAM oligomers was 50 μM.

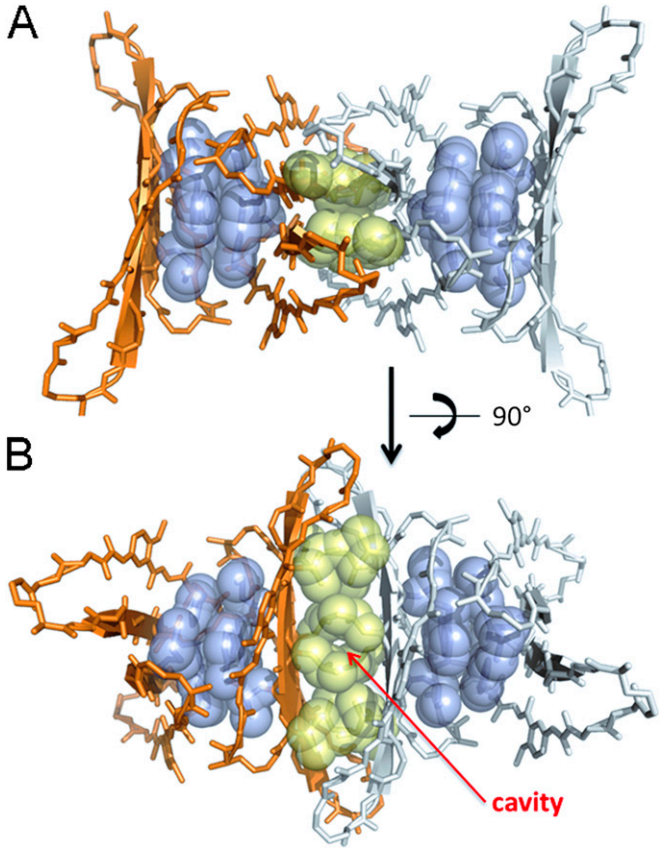

Fig. S5. Interface between two BAM ($A\beta_{30-36}$) cylindrin-like oligomers in the crystal. (*A*) Two cylindrin-like oligomers derived from the structure of fibril-forming BAM ($A\beta_{30-36}$) in the crystal are shown (one in orange and the other in gray). Within each cylindrin-like structure, hydrophobic side chains Phe and Met contributing to the tightly packed core of the β-barrel are highlighted as blue spheres. The buried surface area of these core residues is 524 $Å^2$, and Pi-Pi stacking between two pairs of Phe side chains makes a tightly packed interface in the β-barrel core, which is confirmed by its high shape complementarity (0.78). The interface between two oligomers formed by apolar side chains Leu, Ile, and Val is depicted as yellow spheres. The buried surface area of this interface is 515 $Å^2$, and its shape complementarity (0.51) is lower than the shape complementarity of typical oligomeric interfaces between globular proteins (from 0.70 to 0.74). This finding indicates that, compared with the interface formed within the cylindrin-like oligomer, this interface is not a strong one for BAM ($A\beta_{30-36}$) self-assembly. However, given the high buried surface area, this interface might play a role in the further association of cylindrin-like oligomers into higher-order structures. (*B*) A view 90° from *A* shows the center of the interface between the cylindrin-like oligomers. The cavity in the center, indicated by the red arrow, highlights the poor packing of the interface. This finding illustrates that the interface between two oligomers (yellow) is much less tightly packed than the interface within oligomers (purple).

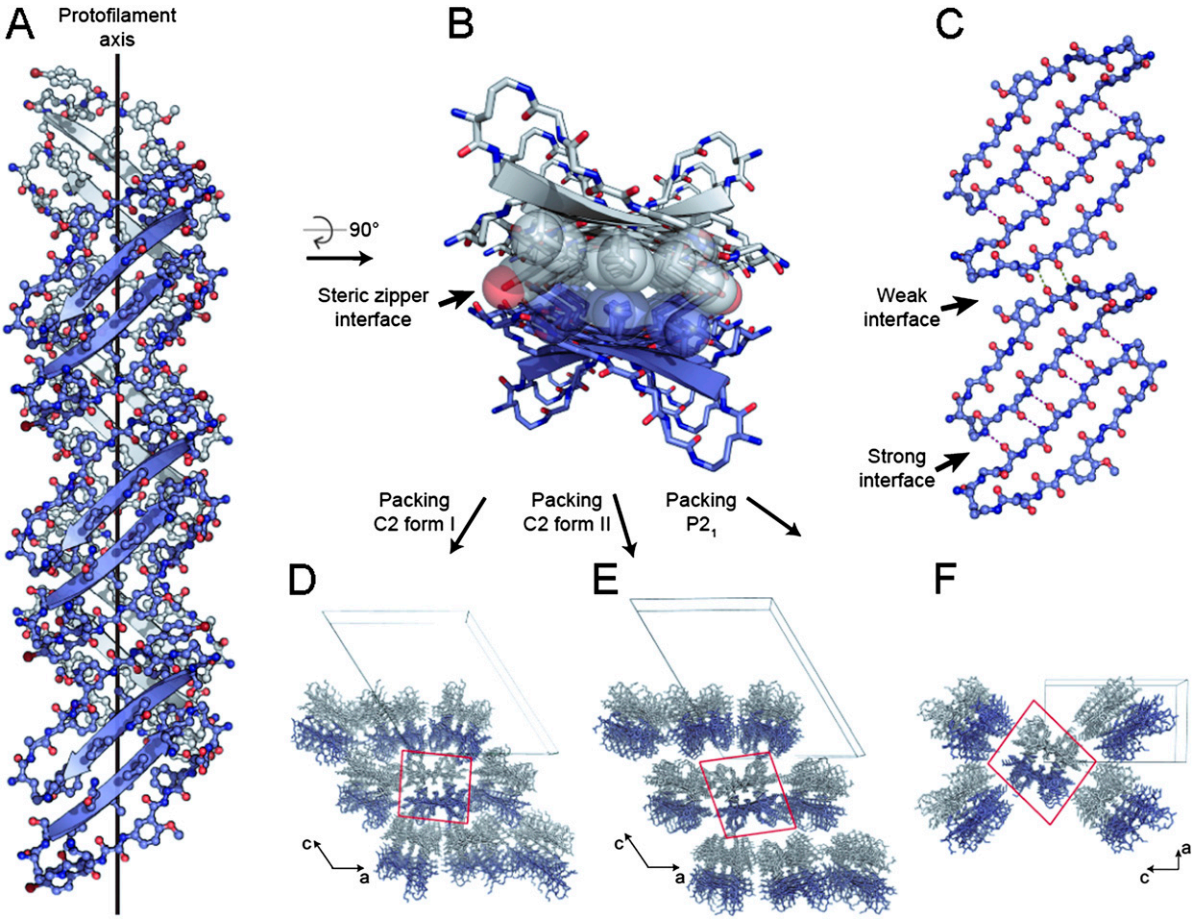

Fig. S6. BAM ($Tau_{305–311}$) exhibits out-of-register fibrillar packing in three different crystal types. (*A*) A view perpendicular to the protofilament axis. Note that the strands are not perpendicular to the protofilament axis and the out-of-register contacts between dimers within a sheet. (*B*) A view 90° from *A* down the protofilament axis showing the steric interface. Side chains contributing to the steric interface are shown in space-filling representation. For clarity, other side chains are omitted. (*C*) Topology of a single sheet. Only backbone atoms are shown. Hydrogen bonds at weak and strong interfaces are shown by yellow and magenta dotted lines, respectively. (*D–F*) Crystal packing of BAM ($Tau_{305–311}$). Shown are three different crystal packings with otherwise very similar structure. Unit cell boundaries are shown by black lines with a coordinate system in the corner showing the orientation. Inside the red boxes are single pairs of sheets that constitute a fibril as shown in *A*.

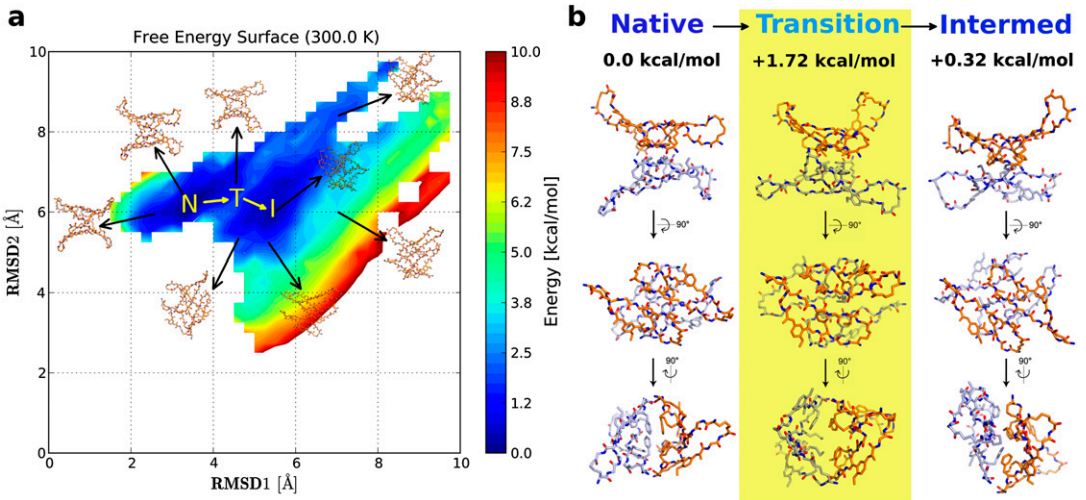

Fig. S7. 2D Gibbs free energy heat map describes the conversion pathway from native cylindrin-like state (N) to out-of-register β-sheets intermediate state (I). (*A*) The Gibbs free energy profile was explored by a series of umbrella sampling simulations along the structural conversion pathway, and a heat map was computed along the two chosen reaction coordinates. RMSD1, rmsd from the cylindrin-like structure; RMSD2, rmsd from the pair of β-sheets structure. Representative structures of several free energy basins are presented. Along the 2D energy heat map, two stable basins representing the N and I states and a local minimal saddle point representing the transition (T) state are highlighted. These three important states shown in *B*, from the N state (0.0 kcal/mol-of-oligomer) to the T state (+1.7 kcal/mol-of-oligomer) to the I state (+0.3 kcal/mol-of-oligomer) constitute a possible minimal free energy pathway. The low activation energy (1.7 kcal/mol) of this minimal free energy pathway is equivalent to ∼3 RT at 300 K, indicating a ready conversion among the N, T, and I states.

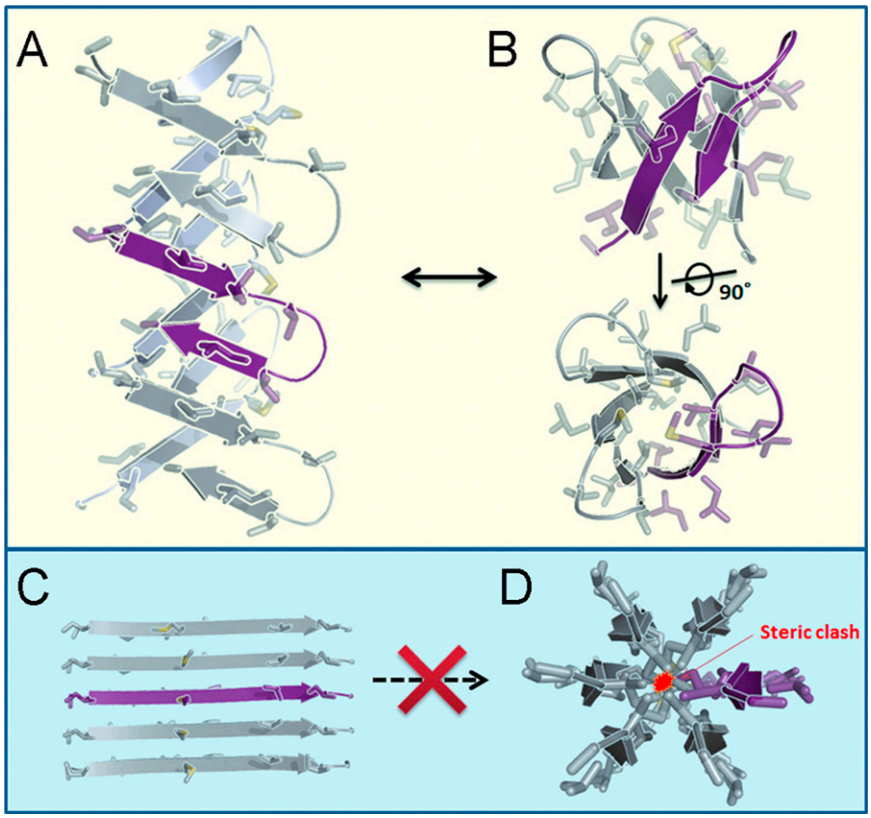

Fig. S8. Out-of-register fibril and cylindrin-like oligomer models of $A\beta_{1-42}$ show that the C-terminal segment (30–42) of Aβ is compatible with out-of-register oligomer and fibril structures. (*A*) Out-of-register fibril model viewed perpendicular to the fibril axis. (*B*) The cylindrin-like oligomer model viewed both perpendicular to (up) and along (low) the cylindrin axis. The building block of both models is a β-hairpin formed by the C-terminal segment of $A\beta_{1-42}$ (purple). Out-of-register fibrils and cylindrin-like oligomers share the same out-of-register β-strand packing, suggesting potential interconversion between these species. (*C*) The NMR structure of the C-terminal segment (30–42) of Aβ (Protein Data Bank ID code 2BEG) shows in-register β-strand packing in the Aβ fibril. (*D*) The hypothetical model of in-register cylindrin-like oligomer, which is viewed along the cylindrin axis, is built by rolling the single in-register β-strands derived from *C*. The steric clash inside the cylindrin is highlighted, indicating that in-register β-strands are not capable of forming a cylindrin-like oligomer.

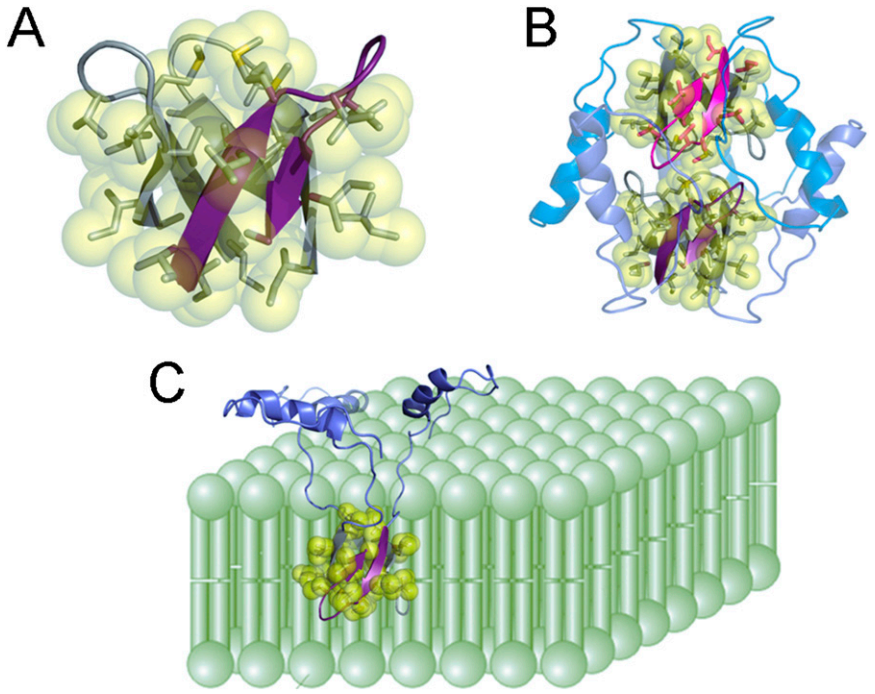

Fig. S9. A depiction of the potential for membrane insertion of the $A\beta_{1-42}$ cylindrin-like oligomer model. (*A*) The cylindrin-like, out-of-register oligomer model of the C-terminal segment (30–42) of $A\beta_{1-42}$ in space-filling representation shows that the solvent-exposed surface of the cylindrin is highly apolar. The oligomer is formed by three copies of the C-terminal segment (30–42), one of which is colored purple. (*B*) One possible model of the full-length $A\beta_{1-42}$ cylindrin-like oligomer in solution. The apolar cylindrin core formed by the C-terminal segment (30–42) is surrounded by the N-terminal segments (colored in violet for the lower cylindrin and blue for the upper cylindrin), with structure that is derived from the partially folded NMR structure (Protein Data Bank 2LFM). Apolar residues (Y10, L17, F19, and F20) of the N terminus stabilize the hydrophobic surface of the cylindrin. Two cylindrins stack on top of each other to form a homodimer, and therefore, R5 and D7 from opposing cylindrins form an intermolecular salt bridge to stabilize the N-terminal α-helices. (*C*) To insert into the membrane, the surrounding N-terminal region moves away from the apolar cylindrin core, exposing the latter to insert into the phospholipid bilayer. This insertion of the apolar cylindrin core might trigger the disruption of membranes.

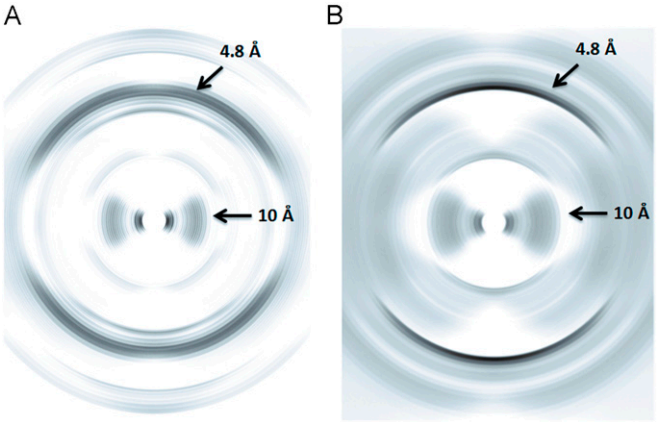

Fig. S10. The fibril diffraction pattern of imperfectly aligned out-of-register fibrils appears similar to the diffraction pattern of an in-register fibril. The simulated fibril diffraction patterns of a hypothetical FSKDWSFYLLY out-of-register fibril model (*A*) and an in-register fibril model (*B*) after a 60° radial blur shows that imperfect alignment of fibrils could distort the diffraction pattern to the extent that it could be indistinguishable from an in-register fibril. An out-of-register fibril is expected to give a split meridional reflection at ∼4.8 Å. However, the splitting can become indistinct if the fibril alignment is not perfect, producing the appearance of a conventional cross-β diffraction pattern. Note that the out-of-register pattern (*A*) is virtually indistinguishable from the diffraction pattern derived from in-register fibrils (*B*). Here, the effect of disorder in aligned fibrils was mimicked by introducing a 60° radial blur to the simulated fibril diffraction pattern. In conclusion, the lack of alignment in fibril samples can conceal the possibility that not all have in-register cross-β structure. Some can be out-of-register with acute crossing angles between β-strands of adjacent sheets.

Table S1. Statistics of X-ray data collection and refinement for the segment KDWSFY ($\beta_2m_{58–63}$) that forms an out-of-register amyloid-like protofilament

	KDWSFY (native)	KDWSFY (iodide)
Crystal parameters		
Space group	$P6_1$	$P6_1$
Cell dimensions		
a, *b*, *c* (Å)	62.4, 62.4, 11.7	62.1, 62.1, 11.8
α, β, γ (°)	90, 90, 120	90, 90, 120
Molecules (asymmetric units)	4	4
Data collection		
Synchrotron beam line	APS (24-ID-C)	APS (24-ID-C)
Wavelength (Å)	0.7749	1.4760
Resolution (Å)	0.97	1.65
Reflections observed/unique	79,026/15,850	26,225/6,023
Completeness (%)	98.9 (99.9)	98.7 (88.7)
R_{merge} (%)*	6.9 (48.8)	6.3 (10.0)
<I/σI>	14.1 (3.8)	17.3 (8.7)
Refinement		
Resolution (Å)	18.0–0.97	
R_{work} (%)†	11.2 (15.0)	
R_{free} (%)‡	13.1 (17.1)	
Number of non-H atoms		
Protein	600	
Nonprotein	95	
Overall B factors	11	
rms deviation		
Bond length (Å)	0.010	
Bond angle (°)	1.417	

Values in parentheses correspond to the highest resolution shell.

*$R_{merge} = \Sigma \mid I - \langle I \rangle \mid / \Sigma I$.

†$R_{work} = \Sigma \mid F_o - F_c \mid / \Sigma F_o$.

‡$R_{free} = \Sigma \mid F_o - F_c \mid / \Sigma F_o$ calculated using a random set containing 5% reflections that were not included throughout structure refinement.

Table S2. Comparison of KDWSFY fibril cytotoxicity (shaded) with cytotoxicity of four in-register fibrils (unshaded) by Student *t* test (one sided, right tail)

Cell line: HeLa	Average of cell viability (n = 4)	SD (σ)	Compare with KDWSFY	
			t value	*P* value
KDWSFY	0.77	0.05	—	—
AIIGLMV ($Ab_{30–36}$)	0.98	0.05	6.4	4E-04
SSTNVG ($IAPP_{28–33}$)	1.03	0.02	11	2E-05
VQIVYK ($Tau_{306–311}$)	0.92	0.03	5.2	10E-04
NFLVHS ($IAPP_{14–19}$)	0.94	0.03	6.5	3E-04

Note that KDWSFY fibrils are significantly more toxic than in-register fibrils (largest $P < 0.001$).

Table S3. Comparison of cytotoxicity of fibril-forming BAMs (unshaded) with cytotoxicity of nonfibril-forming BAMs (shaded) by Student *t* test (one sided, left tail)

Cell line: PC12	Average of cell viability (n = 4)	SD (σ)	Compare with BAM ($IAPP_{26–32}$)		Compare with BAM ($Aβ_{16–22}$)	
			t value	*P* value	*t* value	*P* value
BAM ($Aβ_{30–36}$)	0.59	0.03	−22	7E-08	−24	5E-08
BAM ($β_2m_{62–68}$)	0.86	0.06	−4.2	3E-03	−3.4	10E-03
BAM ($IAPP_{11–17}$)	0.40	0.02	−37	2E-09	−43	7E-10
BAM ($IAPP_{26–32}$)	1.01	0.03	—	—	2.4	4E-02
BAM ($Aβ_{16–22}$)	0.97	0.02	−2.4	4E-02	—	—

Note that fibril-forming BAMs are significantly more toxic than nonfibril-forming BAMs (largest $P < 0.01$).

Table S4. Statistics of X-ray data collection and refinement for fibril-forming BAMs

	BAM ($Tau_{305–311}$) (form I)	BAM ($Tau_{305–311}$) (form II)	BAM ($Tau_{305–311}$) (form III)	BAM ($β_2m_{62–68}$)
Crystal parameters				
Space group	C2	C2	$P2_1$	C2
Cell dimensions				
a, *b*, *c* (Å)	58.3, 25.3, 50.8	69.0, 25.4, 53.5	30.4, 25.4, 52.5	67.0, 40.8, 24.0
α, β, γ (°)	90, 122.2, 90	90, 120.1, 90	90, 91.2, 90	90, 98.8, 90
Molecules (asymmetric units)	4	4	4	4
Data collection				
Synchrotron beam line	APS (24-ID-C)	APS (24-ID-C)	APS (24-ID-C)	APS (24-ID-C)
Wavelength (Å)	0.9161	0.9195	0.9795	0.9795
Resolution (Å)	1.75	1.65	1.82	1.70
Reflections observed/unique	37,743/12,362	39,206/18,614	24,240/12,975	21,125/6,471
Completeness (%)	99.0 (98.7)	97.9 (98.1)	96.5 (96.2)	91.5 (64.5)
R_{merge} (%)*	8.6 (42.4)	9.9 (57.5)	5.6 (41.1)	10.4 (53.0)
<I/σI>	7.8 (2.5)	7.3 (1.9)	10.3 (2.5)	10.0 (2.4)
Refinement				
Resolution (Å)	18.2–1.75	19.4–1.65	18.3–1.82	19.4–1.70
R_{work} (%)†	18.5 (15.4)	20.9 (21.9)	18.2 (16.9)	22.8 (19.4)
R_{free} (%)‡	22.1 (22.8)	25.5 (25.2)	22.9 (21.7)	25.8 (21.9)
Number of non-H atoms				
Macrocycle	547	564	560	540
Solvent	79	133	121	32
Overall B factors	19	21	30	18
rms deviation				
Bond length (Å)	0.010	0.010	0.010	0.008
Bond angle (°)	1.290	1.270	1.380	0.960

Values in parentheses correspond to the highest resolution shell.

*$R_{merge} = \Sigma \mid I - \langle I \rangle \mid / \Sigma I$.

†$R_{work} = \Sigma \mid F_o - F_c \mid / \Sigma F_o$.

‡$R_{free} = \Sigma \mid F_o - F_c \mid / \Sigma F_o$ calculated using a random set containing 5% reflections that were not included throughout structure refinement.

Table S5. Correlation between BAMs fibril-forming capability and the total energy/shape complementarity of BAMs fibril models

BAM	Grafted residues R_1–R_7	Grafted residues R_8–R_{11}	Fibril formation	Total energy*	Shape complementarity†	Energy from strong interface‡	Energy from weak interface§	Nonbond energy¶	Solvation energy‖	H-bond energy	Buried surface area**	SASA packing score††
BAM (β_2m_{62-68})	FYLLYYT	KNSA	+	−93	0.78	−0.64	−0.40	−106	64	−51	871	0.8
BAM ($IAPP_{11-17}$)	RLANFLV	KFYK	+	−83	0.73	−0.57	−0.33	−107	71	−47	927	0.6
BAM ($Tau_{305-311}$)	SVQIVYK	EFYK	+	−82	0.80	−0.54	−0.29	−88	47	−41	607	0.4
BAM ($A\beta_{30-36}$)	AIIGLMV	KFYK	+	−75	0.62	−0.54	−0.33	−81	50	−44	668	0.4
BAM ($A\beta_{16-22}$)	KLVFFAE	KLIE	–	−74	0.50	−0.48	−0.29	−97	67	−44	788	0.5
BAM ($IAPP_{26-32}$)	ILSSTNV	KFYK	–	−70	0.59	−0.47	−0.38	−83	61	−49	654	0.5
BAM ($hPrP_{116-122}$)	AAAGAVV	KFYK	–	−70	0.50	−0.53	−0.34	−74	50	−46	716	0.5
BAM ($Sup35_{7-13}$)	GQQNNQY	KFYK	–	−66	0.48	−0.39	−0.26	−90	73	−49	849	0.4
BAM (α-Syn_{75-81})	TAVANKT	VFYK	–	−62	0.50	−0.35	−0.22	−72	55	−45	322	0.4

To address what actually drives the association of out-of-register β-strands, we performed Rosetta modeling with symmetry restraints. The lowest energy model of each BAM fibril is built by the Rosetta symmetry module (*SI Materials and Methods*). The ability of BAMs with different sequences in the recognition R_1–R_7 (column 2) and blocking strands R_8–R_{11} (column 3) to form fibrils is shown in column 4. The fibril-forming capacity of BAMs correlates well with low energy and high shape complementarity (SC) of the fibril models. The top four BAMs form fibrils (labeled in red) with favorable total energy (column 5), the sum of nonbond LJ potential, LK salvation, H bond energy, and SC scored by CCP4 (column 6). The other five BAMs, with less favorable total energies and poor SC values, fail to form fibrils in solution. We were able to further localize the energy contributions in BAMs fibril models: the major contributor of binding energy is the steric zipper-packing and hydrogen-bonding interactions at the strong H-bond interface between recognition strands (column 7). The energy contributions determine whether BAMs form fibrils. Interactions from the weak H-bond interface formed by blocking strands make smaller contributions. Moreover, some additional parameters, including SC score, buried surface area (column 12), and solvent-accessible surface area (SASA) packing score (column 13), correlate well with fibril formation of BAMs. These findings indicate that, whereas both van der Waals interactions from side chains and H-bond interactions from backbones drive fibrillation, the van der Waals interactions of the steric zipper interface determine out-of-register β-strand packing.

*Total energy is the sum of nonbond energy, salvation, and H-bond energy. The unit of all energy scores is in kilocalories $mole^{-1}$.

†The SC score is calculated by the CCP4 package. The SC scores evaluate the packing of the steric zipper interface in the BAM fibrils, and the score is 1.0 for perfect packing.

‡Energy per atom of residues R_1–R_7 of the recognition strand that constitutes strong H-bond interfaces along the fibril axis.

§Energy per atom of residues R_8–R_{11} of the blocking strand that forms weak H-bond interfaces along the fibril axis.

¶Nonbond Lennard–Jones potential.

‖LK-implicit solvation energy.

**Buried surface area (angstrom^2) of the macrocylic dimers between the adjacent β-sheets (intersheet) and at the weak interface between the blocking strands (R_8–R_{11}) stacking within the same β-sheet (intrasheet).

††SASA packing as described in *SI Materials and Methods*.